Base Station Clock Offset of Cellular Measurements and Its Impact on Positioning

Ivan Lapin, Gonzalo Seco-Granados, *Fellow, IEEE*, Jaron Samson, and José Antonio Garcia-Molina

***Abstract*—Positioning with cellular networks can serve as a backup or as a complement to the Global Navigation Satellite System (GNSS), making it relevant for autonomous vehicle navigation with integrity monitoring. The user equipment (UE) can compute its position with cellular measurements that are obtained by tracking the code phase and carrier phase of received cellular signals. Integrity monitoring techniques require rigorous characterization of the cellular measurements and their corresponding error models. An important component of the downlink code phase and carrier phase measurements is the base station (BS) clock offset, which represents the deviation of the BS clock from a reference clock. Leaving the BS clock offset uncorrected or using a clock prediction model that does not fit the clock dynamics properly can result in an undesirable degradation of the positioning performance. In this work, the BS clock offset is studied using cellular measurements collected by tracking the cell-specific reference signal (CRS) of two commercially operated long-term evolution (LTE) BS uninterruptedly for eleven days. To avoid cycle slips or losses of the signal lock during high clock dynamics, the optimal bandwidths of the receiver tracking loop filters are first determined via simulation. The analysis of the collected carrier phase measurements shows that the main contributor to the BS clock offset is the occurrence of regular oscillator frequency jumps, which are sudden changes in the clock oscillator frequency. The jumps could be caused by a periodic clock steering mechanism keeping the BS clocks synchronized to the primary clock reference. The code-minus-carrier (CMC) analysis shows that both monitored stations adjust the code phase and carrier phase coherently. The impact of the BS clock offset on positioning is studied in a simulated terrestrial scenario in which the user relies on cellular measurements to coast during GNSS unavailability. The results show that the clock prediction model can significantly reduce the horizontal position error (HPE) when compared to the uncorrected BS clock offset.**

***Index Terms*—5G NR, cellular positioning, base station clock offset, LTE, oscillator frequency jump.**

I. Introduction

THE fourth-generation (4G) long-term evolution (LTE) and fifth-generation (5G) new radio (NR) cellular systems have evolved into relevant sources of positioning thanks to their favorable signal characteristics and good coverage in urban environments [1]. Cellular signals are relevant for autonomous vehicle navigation as they can serve, along with other sensors, as a backup or as a complement to the Global Navigation Satellite System (GNSS) [2], [3], [4], [5], [6]. Cellular signals are also relevant for autonomous integrity monitoring, whose goal is to quantify the confidence of the navigation solution and to detect and reject incorrect measurements to meet a certain integrity risk [7]. Hybridization of GNSS with cellular measurements was shown to lower the protection levels (PLs) [8], [9], improve the availability of the PLs [10], or improve the fault detection rate [11].

Integrity monitoring techniques require rigorous characterization of the nominal measurement error model along with the probabilities of the model failing to bound the nominal errors. Such models have been well established in GNSS through commitments made by GNSS core constellations [12], [13] and extensive error characterization studies and campaigns [14], [15], [16], [17], [18], [19]. Notable examples of integrity concepts in GNSS relying on such models include the satellite-based augmentation system (SBAS) [20] or the receiver autonomous integrity monitoring (RAIM) [21]. Similarly to GNSS, the incorporation of cellular signals into integrity monitoring requires extensive studies of measurement errors along with performance commitments of cellular networks. However, unlike GNSS, the error models of cellular signals remain widely unexplored.

The user equipment (UE) can compute its position with cellular measurements that are obtained by tracking the code phase and carrier phase of received cellular signals. In terrestrial scenarios, these measurements correspond to the geometrical distance between the transmitter and receiver, transmitter and receiver clocks, various instrumental delays in the signal processing chain, and measurement errors. An important component of the downlink code phase and carrier phase measurements is the base station (BS) clock offset, which represents the deviation of the BS clock from a reference clock. The clock of a typical cellular BS has lower stability than the atomic clock used onboard a GNSS satellite. 3GPP specifications of 5G NR [22] and LTE [23] define the carrier frequency error as the measure of the difference between the actual BS transmit frequency and the assigned frequency, which should stay for both technologies within ± 50 ppb for wide area BS and ± 100 ppb for medium range and local area BS over a period of 1 ms. Similarly to real-time non-differential methods in GNSS, the BS clock offset can be estimated and predicted using clock prediction

Manuscript received 12 December 2023; revised 3 April 2024; accepted 28 May 2024. Date of publication 4 June 2024; date of current version 17 October 2024. This work was supported in part by the ICREA Academia Program, the Catalan Project 2021 SGR 00737, and in part by the Spanish R+D project PID2020-118984GB-I00. The review of this article was coordinated by Dr. Jiguang He. *(Corresponding author: Ivan Lapin.)*

Ivan Lapin, Jaron Samson, and José Antonio Garcia-Molina are with the Radio Navigation Systems and Techniques Section of the Radio Frequency Systems Division, European Space Agency, 2201 AZ Noordwijk, The Netherlands (e-mail: ivan.lapin@esa.int).

Gonzalo Seco-Granados is with the Department of Telecommunications and Systems Engineering, Universitat Autonoma de Barcelona, 08193 Bellaterra, Spain.

Digital Object Identifier 10.1109/TVT.2024.3409088

models [24]. This estimation can be performed by the cellular network, external augmentation service, or one or several users during GNSS availability. The clock stability of commercially operated BS was previously studied by Winter et al. in [25]. The authors analyzed downlink cellular measurements collected from three network operators and showed that the BS clock offset can vary significantly between different operators but remains similar for stations from the same operator. Tedeschini et al. showed in [26] that a clock offset resulting from an inaccurate synchronization among 5G NR BS has a major impact on the position accuracy when code phase measurements are used, requiring clock bias correction.

The study of the BS clock offset requires tracking the code phase and carrier phase of the received cellular signals over sufficiently long periods. GNSS receivers rely traditionally on a computationally inexpensive closed-loop receiver architecture implementing the delay-locked loop (DLL) and phase-locked loop (PLL) to obtain the respective measurements [21]. Various LTE and 5G NR software positioning receivers based on the closed-loop architecture have been presented [27], [28], [29], [30], [31]. These receivers were shown to operate in a post-processing mode, where the captured baseband signal is first stored on a drive before being processed. Since the source code of the receivers has not been shared publicly, their real-time capabilities remain unclear. A real-time receiver accesses directly the software-defined radio (SDR) baseband stream, allowing it to process signals continuously over arbitrarily long periods. STARE, a publicly available real-time SofTwAre REceiver for positioning with the LTE and 5G NR cellular downlink signals, was previously developed to support signal monitoring or long positioning field trials spanning hours or days [32].

LTE and 5G NR cellular downlink waveforms utilize orthogonal frequency division multiplexing (OFDM) and contain various signals that can be used to estimate the code phase and carrier phase measurements. A signal tailored for positioning, called the positioning reference signal (PRS) [33], [34], would preferably be used for this purpose. However, the PRS requires a specific network configuration and user subscription, reducing its availability for monitoring. Alternatively, signals that are always transmitted by the network and do not require a user subscription may be used to obtain the necessary measurements, allowing for greater signal availability. One such signal in LTE systems, called the cell-specific reference signal (CRS), has been widely used for positioning and monitoring purposes [32], [35], [36]. The CRS is suitable to study the BS clock offset as it is mapped to the same OFDM waveform as the PRS.

In this paper, the BS clock offset of cellular measurements and its impact on positioning is studied using data collected by a software receiver. The main contributions of the paper are summarized as follows:

i) Determination of the optimal bandwidths of tracking loop filters, allowing the receiver to track the BS clock offset during oscillator frequency jumps without cycle slips or losses of the signal lock.
ii) A detailed analysis of the carrier phase measurements collected from two commercially operated cellular BS during eleven days.
iii) Identification of the oscillator frequency jump as the main contributor to the BS clock offset.
iv) Description of a clock prediction model allowing to estimate and predict the BS clock offset and mitigate the impact of the oscillator frequency jumps.
v) Evaluation of the positioning performance in a simulated terrestrial scenario in which the user relies on cellular measurements to coast during GNSS unavailability.

The remainder of the paper is organized as follows. Section II presents the receiver design and relevant evaluation metrics. Section III studies the optimal configuration of tracking loops allowing the receiver to track the BS clock offset during oscillator frequency jumps. The results of monitoring of two base stations are evaluated in Section IV. Section V studies the impact of oscillator frequency jumps on cellular positioning and its mitigation using clock prediction models. Conclusions are given in Section VI.

Notation: Matrices are denoted as uppercase boldface letters, such as $\mathbf{X} \in \mathbb{C}^{M\times N}$. Column vectors are denoted as lowercase boldface letters, such as $\mathbf{x} \in \mathbb{C}^{M\times 1}$. $\mathbf{X} = \mathrm{diag}(\mathbf{x})$ denotes a $P \times P$ diagonal matrix whose diagonal values are equal to $\mathbf{x} \in \mathbb{C}^{P\times 1}$. The operators $(\cdot)^{\mathrm{T}}$ and $(\cdot)^{-1}$ denote the transpose and the inverse of a matrix, respectively. $|\cdot|$, $\angle(\cdot)$, and $(\cdot)^*$ denote the absolute value, the argument, and the conjugate of a complex number, respectively. The operator $\lceil\cdot\rceil$ denotes a ceiling function.

II. Methodology

A. Receiver Design

STARE is a real-time SofTwAre REceiver for positioning and monitoring of the 5G NR and LTE downlink signals developed by the European Space Agency (ESA) [32]. The real-time operation is achieved by interfacing directly with the software-defined radio (SDR). STARE supports multi-channel SDRs and parallel execution of an arbitrary number of tracking channels. Each tracking channel acquires and tracks the carrier frequency offset (CFO) and sample timing offset (STO) of the desired signal and outputs the related code phase $\hat{\upsilon}$, Doppler frequency $\hat{f}_{\mathrm{D}}$, and carrier phase $\hat{\phi}$ measurements. The tracking channel also outputs the estimated signal-to-noise ratio (SNR). Each tracking channel operates independently in three stages that are inspired by the previous works on LTE and 5G NR positioning receivers [27], [28], [29], [30], [31]:

a) *Coarse acquisition stage* initializes the CFO and STO estimates and establishes the timing synchronization to the downlink signal, relying on the correlation properties of the cyclic prefix (CP) and synchronization signals.
b) *Fine acquisition stage* refines the initial estimates to allow the tracking loops to acquire the signal lock, relying on the ESPRIT super-resolution algorithm with a path selection criterion based on the SNR.
c) *Tracking stage* keeps continuously updating the estimates using the delay-locked loop (DLL) and phase-locked loop (PLL). The tracking stage outputs the code phase, Doppler frequency, and carrier phase measurements until the signal lock is lost and its re-acquisition is needed.

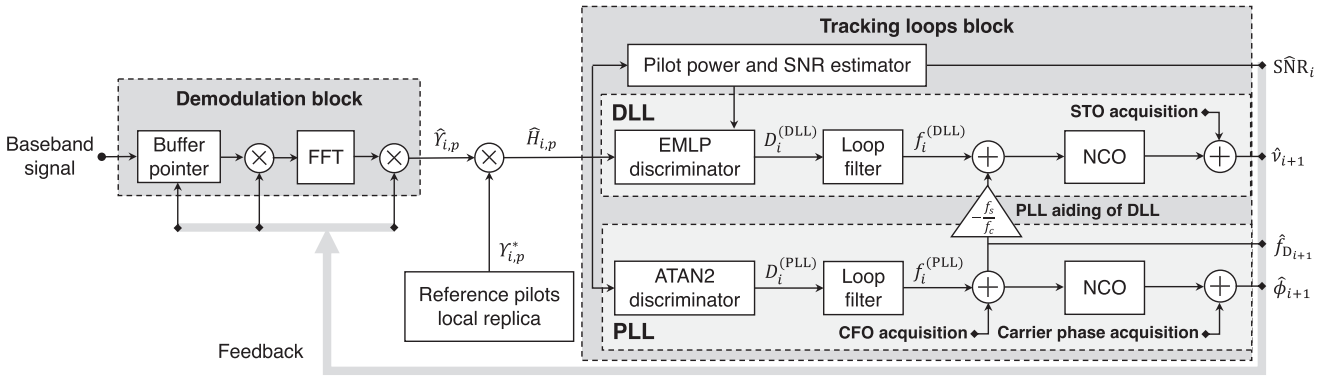

Fig. 1. Block diagram of the tracking stage of STARE. The tracking stage takes place after the initial coarse and fine acquisition of CFO and STO estimates. The design of the tracking stage follows a closed-loop architecture, where the tracking loops (DLL and PLL) keep updating the estimates, which are then fed back to the received signal in the next iteration to maintain the signal lock. The estimated $\hat{\mathrm{SNR}}_i$ belongs to the current channel iteration and the code phase $\hat{\upsilon}_{i+1}$, Doppler frequency $\hat{f}_{\mathrm{D}_{i+1}}$, and carrier phase $\hat{\phi}_{i+1}$ measurements belong to the next iteration. The integer part of the code phase estimate ($\lceil \hat{\upsilon} \rceil$) is used to shift the FFT window in the time domain and the fractional part ($\hat{\upsilon} - \lceil \hat{\upsilon} \rceil$) is applied as a phase rotation of the subcarriers in the frequency domain. The NCO denotes the numerically controlled oscillator in the figure.

The details of the signal processing employed in the coarse and fine acquisition stages are presented in [32]. The block diagram of the tracking stage is shown in Fig. 1. The continuous signal tracking is achieved by a closed-loop architecture where the DLL and PLL estimate the respective residual code phase and carrier phase offsets between the received signal and the locally generated replica. Each tracking loop is composed of three parts: discriminator, loop filter, and numerically controlled oscillator (NCO). The main role of the tracking loops is to drive the discriminator outputs to zero and thus maintain the signal lock. To achieve this, the outputs of the tracking loops are fed back to the received signal in the next loop iteration to remove the estimated offsets.

1) Channel Impulse Response Estimation: The tracking stage relies on the channel frequency response (CFR) that is estimated using pilots mapped to specific OFDM subcarriers as

$$\hat{H}_{i,p} = \hat{\Upsilon}_{i,p} \Upsilon^{*}_{i,p} \in \mathbb{C}, \tag{1}$$

where i is the time index that is incremented with each loop iteration, $p = 0, 1, \ldots, P_i - 1$ is the index of the pilot, P_i is the number of pilots, $\hat{\Upsilon}_{i,p}$ is the received pilot symbol with removed code phase and carrier phase offsets that were estimated in the previous iteration of the tracking loops as shown in Fig. 1, and $\Upsilon_{i,p}$ is the pilot symbol replica at the receiver. The power of the received pilot is assumed to be equal on each subcarrier, so $|\hat{\Upsilon}_{i,p}|^2 = C_i$. The power of each pilot replica at the receiver is unitary, so $|\Upsilon_{i,p}|^2 = 1$. The loop iteration index i is for simplicity omitted for the remainder of the section unless needed.

2) Early-Minus-Late Power Discriminator: The code phase offset between the received signal and the local replica is estimated using the normalized non-coherent early-minus-late power (EMLP) discriminator that is defined as [37]

$$D^{(\mathrm{DLL})}(e_\upsilon, \delta) = \frac{|R(e_\upsilon, -\delta)|^2 - |R(e_\upsilon, \delta)|^2}{C\, k_{\mathrm{EMLP}}(\delta)} \in \mathbb{R}, \tag{2}$$

where the discriminator output is expressed in the number of baseband signal samples, e_υ is the code phase offset of the received signal, δ is the correlator half-spacing, $R(e_\upsilon, -\delta)$ is the output of the early correlator branch, $R(e_\upsilon, +\delta)$ is the output of the late correlator branch, and $k_{\mathrm{EMLP}}(\delta)$ is the dimensionless normalization factor to keep $D^{(\mathrm{DLL})}(e_\upsilon, \delta) \approx e_\upsilon$ when $e_\upsilon \approx 0$. The early and late branches are defined as [38]

$$R(e_\upsilon, \mp\delta) = \frac{1}{P} \sum_{p=0}^{P-1} \hat{H}_p\, e^{-j \frac{2\pi}{N_{\mathrm{FFT}}} (e_\upsilon \pm \delta)\, n_p} \in \mathbb{C}, \tag{3}$$

where n_p is the OFDM subcarrier index of the p-th pilot and N_{FFT} is the FFT length. The normalization factor $k_{\mathrm{EMLP}}(\delta)$ can be expressed as [37]

$$k_{\mathrm{EMLP}}(\delta) = \frac{2\left[1 - \delta\pi\beta \sin(2\pi\beta\delta) - \cos(2\pi\beta\delta)\right]}{(\pi\beta)^2\, \delta^3} \in \mathbb{R}, \tag{4}$$

where $\beta = \frac{P\,\Delta P}{N_{\mathrm{FFT}}}$ is the OFDM waveform factor corresponding to the ratio between the usable signal bandwidth spanned by the pilots and the IFFT/FFT length, and ΔP is the pilot spacing.

3) ATAN2 Discriminator: The carrier phase offset between the received signal and the local replica is estimated using the normalized 2-argument arctangent (ATAN2) discriminator that is defined as [27], [30]

$$D^{(\mathrm{PLL})} = \frac{1}{2\pi} \cdot \angle \left(\sum_{p=0}^{P-1} \hat{H}_p \right) \in \mathbb{R}, \tag{5}$$

where the discriminator output is expressed in the number of cycles of the carrier frequency f_c.

4) Loop Filter: The outputs of the DLL and PLL discriminators are fed to the discrete loop filters to reduce the higher frequency noise components. The loop filter transfer function of the second-order DLL is implemented as

$$f_i^{(\mathrm{DLL})} = f_{i-1}^{(\mathrm{DLL})} + \left(\frac{T_\eta \omega_2^2}{2} + 2\zeta\omega_2 \right) D_i^{(\mathrm{DLL})} + \left(\frac{T_\eta \omega_2^2}{2} - 2\zeta\omega_2 \right) D_{i-1}^{(\mathrm{DLL})} \left[\mathrm{s}^{-1} \right], \tag{6}$$

where $f_i^{(\mathrm{DLL})}$ is the DLL output at the i-th loop iteration, T_η [s] is the loop integration time, ζ is the dimensionless loop damping factor, $D_i^{(\mathrm{DLL})}$ is the discriminator output from (2) at the i-th loop iteration, and ω_2 is the loop natural frequency determined using the loop bandwidth parameter $B_{\mathrm{n}}^{(\mathrm{DLL})}$ [Hz] as

$$\omega_2 = \frac{8\zeta}{4\zeta^2+1} B_{\mathrm{n}}^{(\mathrm{DLL})} \ [\mathrm{Hz}]\,. \tag{7}$$

The loop filter transfer function of the third-order PLL is implemented as

$$\begin{aligned} f_i^{(\mathrm{PLL})} &= 2\, f_{i-1}^{(\mathrm{PLL})} - f_{i-2}^{(\mathrm{PLL})} \\ &\quad + \left(\frac{T_\eta^2 \omega_3^3}{4} + \frac{a T_\eta \omega_3^2}{2} + b\,\omega_3 \right) D_i^{(\mathrm{PLL})} \\ &\quad + \left(\frac{T_\eta^2 \omega_3^3}{2} - 2b\,\omega_3 \right) D_{i-1}^{(\mathrm{PLL})} \\ &\quad + \left(\frac{T_\eta^2 \omega_3^3}{4} - \frac{a T_\eta \omega_3^2}{2} + b\,\omega_3 \right) D_{i-2}^{(\mathrm{PLL})} \\ &\quad \left[\mathrm{s}^{-1}\right], \end{aligned} \tag{8}$$

where $f_i^{(\mathrm{PLL})}$ is the PLL output at the i-th loop iteration, a and b are the dimensionless filter coefficients, $D_i^{(\mathrm{PLL})}$ is the discriminator output from (5) at the i-th loop iteration, and ω_3 is the loop natural frequency determined using the loop bandwidth parameter $B_{\mathrm{n}}^{(\mathrm{PLL})}$ [Hz] as

$$\omega_3 = \frac{4\,(ab-1)}{ab^2+a^2-b} B_{\mathrm{n}}^{(\mathrm{PLL})} \ [\mathrm{Hz}]\,. \tag{9}$$

B. Cycle Slip Detector

Cycle slips are detected by exploiting different polarizations between antenna ports (APs) 0 and 1 as proposed in [39]. The carrier phase measurements are compared with the cycle slip threshold α_{cs} as

$$\left| \hat{\phi}_q^{(\text{AP-0})} - \hat{\phi}_q^{(\text{AP-1})} - \hat{\phi}_0^{(\text{AP-0})} + \hat{\phi}_0^{(\text{AP-1})} \right| \geq \alpha_{\mathrm{cs}}, \tag{10}$$

where $\hat{\phi}_q^{(\text{AP-0})}$ and $\hat{\phi}_q^{(\text{AP-1})}$ are the q-th normalized carrier phase measurements of the two APs within a given measurement set. A cycle slip is detected when α_{cs} is exceeded. The cycle slip threshold is set to $\alpha_{\mathrm{cs}} = 0.5$, which is equivalent to half of the PLL discriminator range.

C. Measurement Model and Base Station Clock Offset

The BS clock offset δt^{s} represents the deviation of the BS clock from a reference clock. It affects both code phase and carrier phase measurements. The code phase measurement can be modeled as

$$\hat{R} = \frac{c}{f_{\mathrm{s}}} \hat{\upsilon} = \rho + c\,(\delta t_{\mathrm{r}} - \delta t^{\mathrm{s}}) + b^{(R)} + m^{(R)} + \epsilon^{(R)} \ [\mathrm{m}]\,, \tag{11}$$

where c is the speed of light, f_{s} is the baseband signal sampling frequency, ρ is the geometric range between the station and the receiver antenna phase centers, δt_{r} is the receiver clock offset, $b^{(R)}$ is the code phase bias, $m^{(R)}$ is the code phase multipath, and $\epsilon^{(R)}$ is the code phase noise. Unlike GNSS, the propagation of terrestrial signals is impacted by neither the ionosphere nor the troposphere, and the corresponding terms are not needed in the model.

The carrier phase measurement can be modeled as

$$\begin{aligned} \hat{\Phi} = \frac{c}{f_{\mathrm{c}}} \hat{\phi} &= \rho + c\,(\delta t_{\mathrm{r}} - \delta t^{\mathrm{s}}) + \lambda N^{(\Phi)} \\ &\quad + b^{(\Phi)} + m^{(\Phi)} + \epsilon^{(\Phi)} \ [\mathrm{m}]\,, \end{aligned} \tag{12}$$

where besides the terms in (11), λ is the carrier wavelength, $N^{(\Phi)}$ is the unknown integer ambiguity of the carrier phase accumulator, $b^{(\Phi)}$ is the carrier phase bias, $m^{(\Phi)}$ is the carrier phase multipath, and $\epsilon^{(\Phi)}$ is the carrier phase noise.

D. Code-Carrier Coherence

The BS clock offset terms in (11) and (12) are equal when the station maintains the coherence between the code phase and carrier phase. The code-carrier coherence can be studied with the code-minus-carrier (CMC) technique, which removes the geometry and common clock errors by subtracting the carrier phase measurement from the corresponding code phase measurement at a given epoch as

$$\begin{aligned} \mathrm{CMC} = \hat{R} - \hat{\Phi} &= m^{(R)} - m^{(\Phi)} + \varepsilon^{(R)} - \varepsilon^{(\Phi)} + b^{(R)} \\ &\quad - \lambda N^{(\Phi)} - b^{(\Phi)} + \Delta_{\delta t^{\mathrm{s}}} \ [\mathrm{m}]\,, \end{aligned} \tag{13}$$

where $\Delta_{\delta t^{\mathrm{s}}}$ represents any difference in the BS clock offset between the code phase and carrier phase measurements. Since the integer ambiguity $N^{(\Phi)}$ and biases $b^{(R)}$ and $b^{(\Phi)}$ in (13) are constant within a measurement set containing no cycle slip or loss of the signal lock between consecutive epochs, and since the carrier phase multipath and noise errors are orders of magnitude smaller than the code phase multipath and noise errors, the mean CMC value can be subtracted within each measurement set to extract the joint effect of multipath, code noise, and BS clock offset as

$$\hat{\mathrm{CMC}} = \mathrm{CMC} - \overline{\mathrm{CMC}} \approx m^{(R)} + \epsilon^{(R)} + \Delta_{\delta t^{\mathrm{s}}} \ [\mathrm{m}]\,. \tag{14}$$

The code-carrier coherence is maintained when the CMC measure in (14) remains bounded and does not diverge.

E. Overlapping Allan Variance and Allan Deviation

The overlapping Allan variance and Allan deviation are measures used to analyze the frequency stability of clocks and oscillators for various periods between samples [40]. The dimensionless overlapping Allan variance $\sigma_{\hat{\phi}}^2(\tau)$ can be estimated using carrier phase measurements as

$$\begin{aligned} \sigma_{\hat{\phi}}^2(\tau) = \sigma_{\hat{\phi}}^2(mT_\eta) &= \frac{1}{2 f_{\mathrm{c}}^2\, m^2\, T_\eta^2\, (Q-2\,m)} \\ &\quad \times \sum_{q=0}^{Q-2m-1} \left(\hat{\phi}_{q+2\,m} - 2\,\hat{\phi}_{q+m} + \hat{\phi}_q \right)^2, \end{aligned} \tag{15}$$

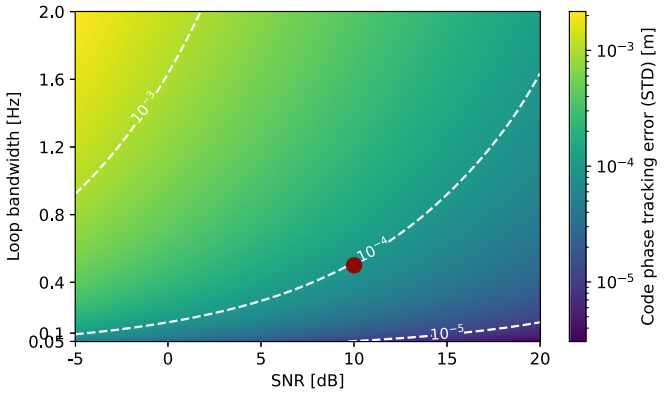

Fig. 2. Standard deviation (STD) of the code phase tracking error for various loop bandwidths and SNRs during a steady-state operation of the second-order DLL. The code phase tracking error is based on simulations in the AWGN channel without multipath. The isolines (10^{-3}, 10^{-4}, and 10^{-5}) in the plot show different orders of the error. The working point of the DLL used for signal monitoring is highlighted with the red circle marker.

where τ is the averaging interval indicating the period between samples, m is the averaging factor, T_η is the basic measurement interval equal to the tracking loop integration time, and Q is the number of samples of normalized carrier phase measurements $\{\hat{\phi}_0, \hat{\phi}_1, \ldots, \hat{\phi}_{Q-1}\}$. The Allan deviation is the square root of the Allan variance and is expressed as $\sigma_{\hat{\phi}}(\tau)$.

III. Optimal Filter Loop Bandwidths

To track high dynamics of BS clocks without cycle slips or losses of the signal lock, the optimal bandwidths of the DLL and PLL are first determined via simulation. A second-order DLL aided by a third-order PLL is selected as the baseline configuration for signal processing. To find the optimal bandwidths, the tracking loops are studied in detail during a nominal steady-state operation and under a simulated oscillator frequency jump. In both cases, a 150 s LTE waveform with a bandwidth of 20 MHz is simulated in the AWGN channel without multipath. The carrier frequency is assumed to be equal to $f_c = 2$ GHz. The receiver is configured to track CRS pilots in the first symbol of every LTE slot, resulting in the loop integration time of $T_\eta = 0.5$ ms. To remove the impact of the acquisition stage on the results, ideal initial estimates are assumed as $\hat{R} = 0$ m, $\hat{\Phi} = 0$ m, and $\hat{f}_D = 0$ Hz.

A. Second-Order Delay-Locked Loop Bandwidth

The optimal bandwidth of the second-order DLL $B_n^{(DLL)}$ is determined in a nominal steady-state operation of the loop. To isolate the performance of the DLL, the PLL is disabled. The SNR ranges from -5 to 25 dB and $B_n^{(DLL)}$ ranges from 0.05 Hz to 2 Hz. The first 50 s of the simulation are discarded to ensure the DLL reaches the steady-state operation. The simulation is repeated 5 times to accumulate 10^6 realizations. The standard deviations of the code phase tracking errors are shown in Fig. 2. The DLL bandwidth of the receiver is set to $B_n^{(DLL)} = 0.5$ Hz to achieve the standard deviation of $\approx 10^{-4}$ m at the SNR of 10 dB. Although such low bandwidth results in reduced sensitivity of the DLL to signal dynamics, this is not considered a problem as high clock dynamics will be tracked by PLL thanks to the PLL aiding mechanism.

TABLE I
Probabilities of Cycle Slips P_{cs} for Various Bandwidths B_n of the Third-Order PLL Under a Simulated Oscillator Frequency Jump

Cycles slipped	P_{cs}		
	$B_n = 14$ Hz	$B_n = 16$ Hz	$B_n = 18$ Hz
0	0.0	1.0	1.0
1	0.9993	0.0	0.0
2	0.0007	0.0	0.0
≥ 3	0.0	0.0	0.0

B. Third-Order Phase-Locked Loop Bandwidth

The optimal bandwidth of the third-order PLL $B_n^{(PLL)}$ is determined under a simulated oscillator frequency jump. The goal is to find the loop bandwidth for which the PLL tracks the maximum assumed jump without a cycle slip or loss of the signal lock. The PLL aiding of DLL is enabled as the performance of the complete tracking block is of interest. Although the 3GPP standards for 5G NR [22] and LTE [23] specify the maximum carrier frequency error as ± 50 ppb over a period of 1 ms, they do not specify the maximum possible instantaneous change in the oscillator frequency. Since the magnitude of the oscillator frequency jump can be theoretically unlimited, an arbitrary maximum jump of ± 16 ppb is assumed, constraining the maximum value of the reliably observable jump in this study.

The oscillator frequency jump is modeled as an instantaneous change in the oscillator frequency at $t = 50$ s in the received signal. The STO is implemented by resampling the waveform after $t = 50$ s with an interpolation/decimation factor of 62361601/62361600, corresponding to

$$\mathrm{STO} = 1 - \frac{62361601}{62361600} = -\frac{1}{62361600} \approx -16.035\,\text{ppb}. \quad (16)$$

To maintain the coherence between the code phase and carrier phase of the signal, the CFO is implemented as

$$\mathrm{CFO} = \mathrm{STO} \cdot f_c \approx -32.071\,\text{Hz}. \quad (17)$$

Based on the results of Section III-A, the DLL bandwidth is set to $B_n^{(DLL)} = 0.5$ Hz. The PLL bandwidth is evaluated for $B_n^{(PLL)} \in \{14, 16, 18\}$ Hz. The probability of a cycle slip is evaluated in 10^3 realizations with the SNR equal to 10 dB. The probabilities of one or multiple cycle slips are summarized in Table I. As can be seen, the loop bandwidth of 14 Hz always results in a cycle slip of one or two cycles when the oscillator frequency jump occurs. No cycle slips are observed for PLL bandwidths of 16 and 18 Hz.

The Doppler frequency, carrier phase, and code phase measurements during a cycle slip when $B_n^{(PLL)} = 14$ Hz are shown in Figs. 3, 4, and 5, respectively. Fig. 3 shows that all three evaluated loop bandwidths estimate correctly the Doppler frequency after the oscillator frequency jump. For the loop bandwidth of $B_n^{(PLL)} = 14$ Hz, an overestimation of the Doppler frequency occurs immediately after the jump, resulting in a cycle slip. The

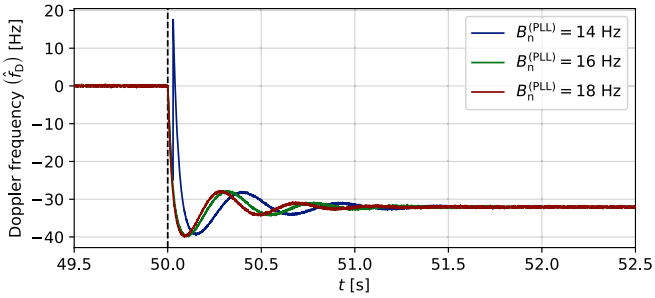

Fig. 3. Doppler frequency measurements for various bandwidths of the third-order PLL. The oscillator frequency jump of ≈ -16.035 ppb, corresponding to CFO ≈ -32.071 Hz, is introduced at $t = 50$ s. The moment of the jump is indicated by the dashed vertical line.

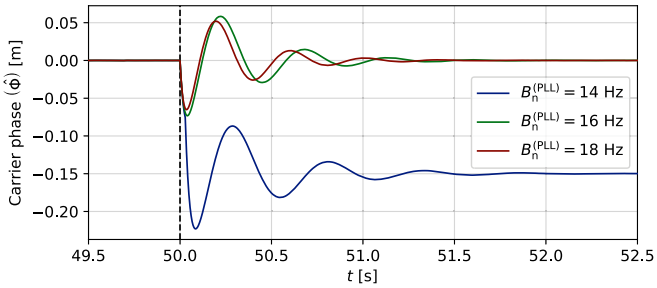

Fig. 4. Carrier phase measurements for various bandwidths of the third-order PLL. The oscillator frequency jump of ≈ -16.035 ppb, corresponding to CFO ≈ -32.071 Hz, is introduced at $t = 50$ s. The moment of the jump is indicated by the dashed vertical line. The jump results in a cycle slip for $B_{\mathrm{n}}^{(\mathrm{PLL})} = 14$ Hz. The drift caused by the oscillator frequency jump after $t = 50$ s is detrended from the plot to facilitate the visualization.

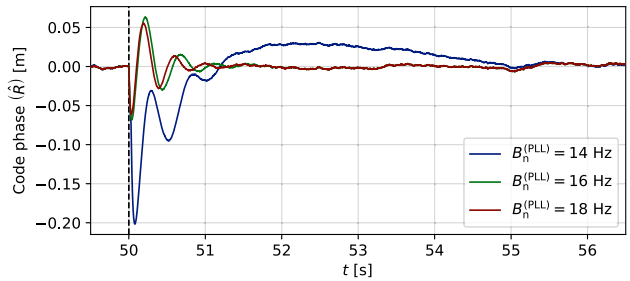

Fig. 5. Code phase measurements for various bandwidths of the third-order PLL. The cycle slip at $t = 50$ s, caused by the oscillator frequency jump indicated by the dashed vertical line, causes a noticeable transition period of the code phase measurements for $B_{\mathrm{n}}^{(\mathrm{PLL})} = 14$ Hz. The drift caused by the oscillator frequency jump after $t = 50$ s is detrended from the plot to facilitate the visualization.

cycle slip of a single cycle equal to -0.15 m is shown in Fig. 4, confirming that the bandwidth of $B_{\mathrm{n}}^{(\mathrm{PLL})} = 14$ Hz is not suitable for observing the ± 16 ppb jumps reliably. Fig. 5 shows that the code phase measurements converge to the correct value for all three bandwidths. To ensure that the tracking loops remain unaffected by the jumps, the PLL bandwidth of the receiver is set to $B_{\mathrm{n}}^{(\mathrm{PLL})} = 18$ Hz.

IV. Monitoring of Base Station Clock Offset

Two commercially operated LTE base stations, further referred to as BS-1 and BS-2, were monitored uninterruptedly for eleven days using a static monitoring setup running STARE. The

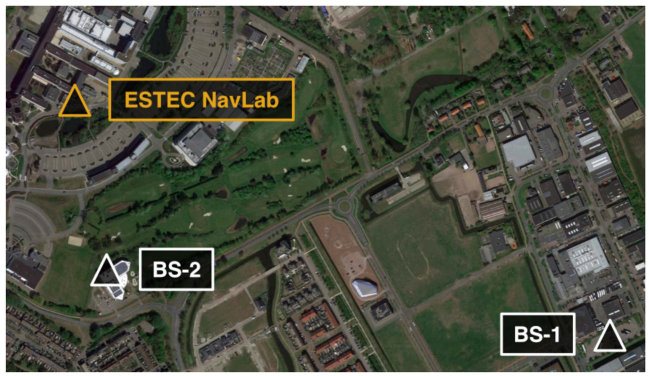

Fig. 6. Approximate locations of the Navigation Laboratory (NavLab) at ESA ESTEC and the monitored base stations BS-1 and BS-2 in its vicinity.

TABLE II
Parameters of the Monitored Cells Including Their Distance From the Laboratory d, Carrier Frequency f_c, Cell ID, Bandwidth B, and Number of Antenna Ports (APs)

BS	d [m]	f_c [MHz]	Cell ID	B [Hz]	N_{FFT}	APs
1	≈ 1100	796	117	10	1024	2
2	≈ 300	806	263	10	1024	2

stations are located in the vicinity of the Navigation Laboratory (NavLab) of the Directorate of Technology, Engineering, and Quality (TEC) at the ESA European Space Research and Technology Centre (ESTEC) in Noordwijk, the Netherlands. The approximate locations of the laboratory and the base stations are shown in Fig. 6. The locations of the antennas are based on the public Dutch antenna register from August 2021 [41]. There is no line-of-sight between the laboratory and the two BS. However, since all antennas are static, the change of the multipath is assumed to be negligible when compared to the BS clock offset. The distance between the monitoring antenna and the antenna of BS-1 and BS-2 is ≈ 1100 m and ≈ 300 m, respectively. Monitoring of BS-1 started on February 4, 2022, 10:32:36. Monitoring of BS-2 started on December 19, 2021, 21:24:28. Parameters of the monitored cells with the strongest signal reception at the receiver are summarized in Table II.

A. Monitoring Setup

The block diagram of the monitoring setup is shown in Fig. 7. The setup includes a single conventional Eightwood LTE magnetic mount antenna with vertical polarization and 3 dBi peak gain, Ettus Universal Software Radio Peripheral (USRP) N310 SDR driven by a highly stable Rubidium reference clock, and a processing unit running Intel Core i9 with 32 threads and 64 GB of memory. The antenna is mounted indoors on the metal window sill of the laboratory. The SDR is connected to the processing unit via the 10 Gigabit copper Ethernet connection, providing a reliable interface to stream the baseband samples.

The configuration parameters of STARE used to monitor both stations are summarized in Table III. A single radio channel with a baseband sampling frequency of 15.36 Msps is connected to the antenna. The radio channel is connected to two tracking

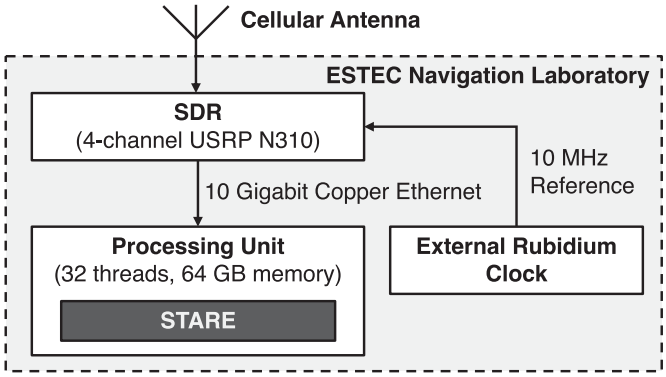

Fig. 7. Block diagram of the LTE signal monitoring setup. The setup includes a single conventional Eightwood LTE magnetic mount antenna with vertical polarization and 3 dBi peak gain, Ettus Universal Software Radio Peripheral (USRP) N310 SDR driven by a highly stable Rubidium reference clock, and a processing unit running Intel Core i9 with 32 threads and 64 GB of memory.

TABLE III
CONFIGURATION PARAMETERS OF STARE USED TO MONITOR THE CLOCKS OF TWO COMMERCIALLY OPERATED BASE STATIONS IN THE VICINITY OF ESTEC NAVIGATION LABORATORY

Radio channel ID	**0**	
Monitored base stations	BS-1, BS-2	
BS-1 / BS-2 carrier frequency f_c [MHz]	796 / 806	
Signal bandwidth B [MHz]	10	
FFT length N_{FFT}	1024	
Sampling frequency f_s [Msps]	15.36	
Tracking channel ID	**0**	**1**
BS-1 / BS-2 cell ID	117 / 263	117 / 263
CP mode	Normal	Normal
Antenna port (AP)	0	1
Algorithm configuration (common for both tracking channels)		
DLL and PLL integration time T_η [ms]	0.5[a]	
DLL / PLL order	2 / 3	
DLL / PLL bandwidth $B_{\text{n}}^{(\text{DLL})}$ / $B_{\text{n}}^{(\text{PLL})}$ [Hz]	0.5 / 18	
DLL filter damping factor ζ	$\frac{1}{\sqrt{2}}$	
PLL filter coefficients a / b	1.1 / 2.4	
DLL EMLP correlator half-spacing δ	0.1	
Code phase / carrier phase tracking threshold	0.39 / 0.25	
SNR tracking threshold [dB]	-20	
SNR tracking threshold duration [s]	5	
Discarded samples from the CP	$\lfloor 0.9 \cdot N_{\text{CP}} \rfloor$	

[a] The CRS pilots in the first symbol of every LTE slot are tracked.

channels, each configured to track the CRS of one of the two APs of the cell. CRS pilots are suitable to study the BS clock offset as they are always transmitted by the station and they do not require a user subscription. The algorithm parameters are identical for both tracking channels. The loop integration time is set to $T_\eta = 0.5$ ms for both DLL and PLL as the CRS pilots in the first symbol of every LTE slot are tracked. Based on the results from Section III, the loop filter bandwidth of the second-order DLL is set to $B_{\text{n}}^{(\text{DLL})} = 0.5$ Hz and the loop filter bandwidth of the third-order PLL is set to $B_{\text{n}}^{(\text{PLL})} = 18$ Hz, providing sufficient responsiveness to track the clock dynamics. During demodulation, 90 % of the CP is discarded before the FFT operation to ensure its application within the OFDM symbol, resulting in $\lfloor 0.9 \cdot N_{\text{CP}} \rfloor$ discarded samples from the CP, where N_{CP} is the number of samples within the CP.

The receiver continuously monitors whether the signal lock is maintained. If the three times standard deviation of the estimated code phase offset or carrier phase offset exceeds a given threshold, the signal lock is considered lost and the corresponding tracking channel repeats the acquisition. The tracking thresholds of the code phase and carrier phase are set to 0.39 and 0.25, respectively. The signal lock is also considered lost when the estimated SNR of the tracked signal drops below -20 dB consecutively for at least 5 s.

B. Processing Steps

The code phase, Doppler frequency, carrier phase, and SNR measurements are collected with a rate of 2 kHz on both APs of each cell and stored on a dedicated drive. The processing steps applied to the collected data are listed as follows:

i) Split the dataset into sets of measurements containing no data gaps, cycle slips, or losses of the signal lock between consecutive epochs. Cycle slips are detected using (10). Losses of the signal lock are detected using the code phase, carrier phase, and SNR tracking thresholds.
ii) Skip the first 10 s from the beginning of each set to ensure convergence of the tracking loops. If no samples are left in the set, skip the set.
iii) Skip the last 10 s from the end of each set to ensure the set does not contain measurements with a low SNR or excessive variance that triggered the tracking thresholds. If no samples are left in the set, skip the set.
iv) In each remaining set, compute the CMC and overlapping Allan deviation.

C. Results and Discussion

In total, 1 897 968 414 and 1 907 985 606 measurements were collected from BS-1 and BS-2, respectively. The SNR measurements for BS-1 and BS-2 are shown in Fig. 8(a) and (b), respectively. It can be seen that the average SNR μ_{SNR} is higher on AP-1 than on AP-0 for both stations, which is attributed to the use of unipolar antenna in the monitoring setup. The mean SNR of BS-1 is lower than the mean SNR of BS-2 for both APs.

1) Base Station Clock Offset: The BS clock offset is studied using the carrier phase measurements instead of the code phase measurements as although ambiguous, the carrier phase measurements are orders of magnitude more precise. The contribution of the receiver clock offset δt_{r} to the carrier phase measurement in (12) is negligible thanks to the use of a highly stable Rubidium reference clock in the monitoring setup. The effects of the carrier phase multipath $m^{(\Phi)}$ and noise $\epsilon^{(\Phi)}$ are negligible compared to the BS clock offset. The geometry ρ and carrier phase bias $b^{(\Phi)}$ are constant thanks to the static placement of the receiving antenna. Within the set of carrier phase measurements without a data gap, cycle slip, or loss of the signal lock, the unknown integer ambiguity $N^{(\Phi)}$ remains constant. Since all terms in (12) except δt^{s} are constant or negligible, the behavior of the BS clock offset can be evaluated for each set by analyzing the raw carrier phase measurements as outputted by the carrier phase accumulator. Although the BS clock offset observed this way is not absolute as not all

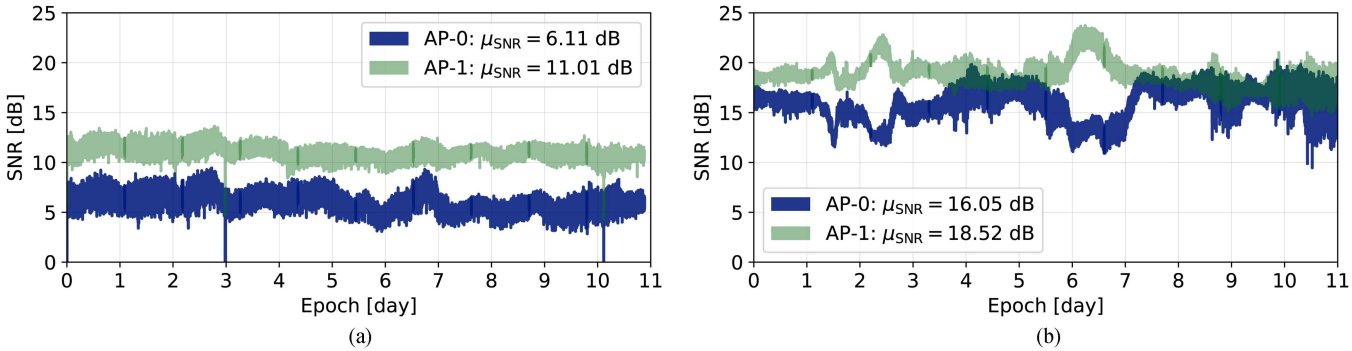

Fig. 8. SNR measurements observed during eleven days of monitoring on both antenna ports (AP-0 and AP-1) of BS-1 (a) and BS-2 (b).

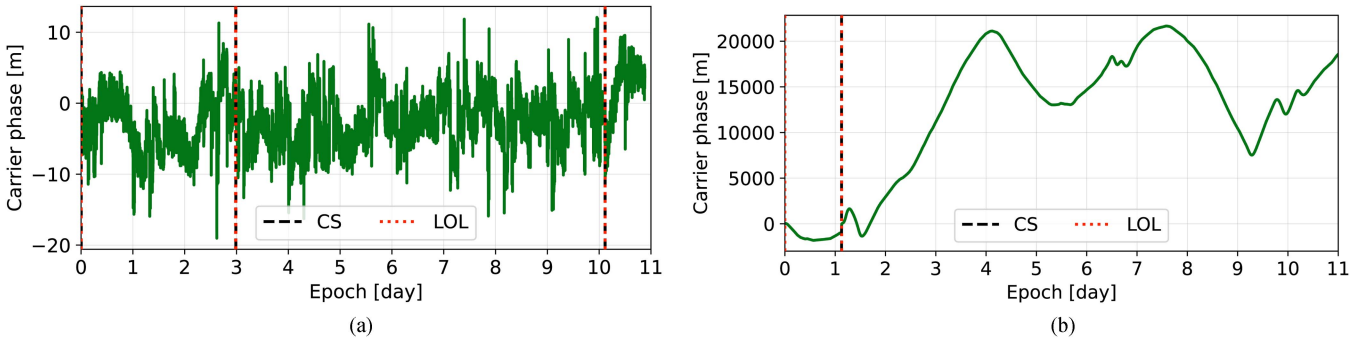

Fig. 9. Carrier phase measurements observed during eleven days of monitoring on AP-1 BS-1 (a) and AP-1 BS-2 (b). Cycle slips (CS) and losses of the signal lock (LOL) are also shown. The carrier phase accumulator is reset to 0 m and a new measurement set is started when the tracking loop is first initialized or when the signal lock is lost.

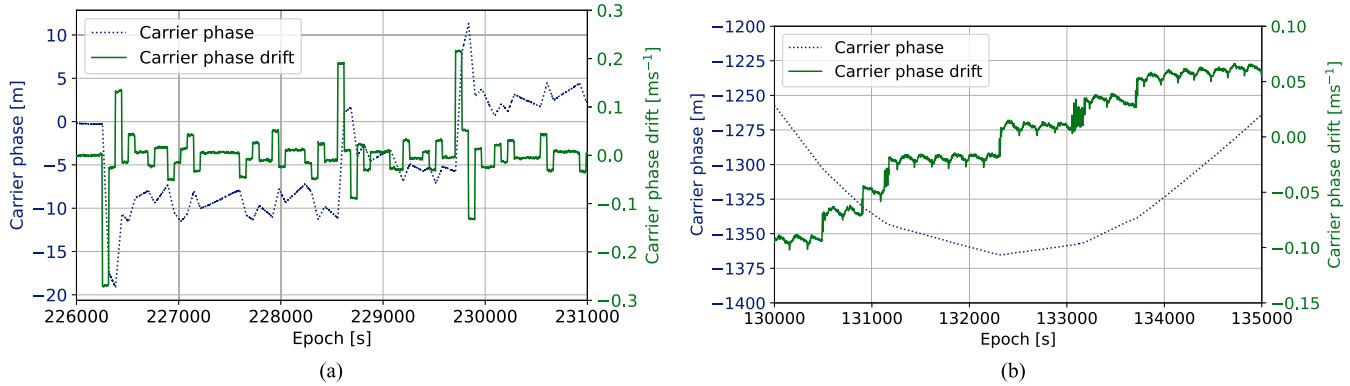

Fig. 10. Carrier phase measurements and drifts during selected intervals of 5000 s revealing regular oscillator frequency jumps on BS-1 (a) and BS-2 (b). The carrier phase drift is estimated by performing a linear regression of the carrier phase measurements over a 5 s sliding window and taking the slope of the regression. The estimated carrier phase drift is aligned with the first carrier phase measurement of the window.

terms are estimated, its relative value is sufficient to analyze the behavior of the clocks. The BS clock offset results obtained by monitoring LTE signals are considered relevant for 5G NR as both technologies are driven by the same requirements for the maximum carrier frequency error [22], [23].

For both stations, only the carrier phase measurements observed on AP-1 are further considered as they are observed under a higher SNR than on AP-0. The carrier phase measurements of BS-1 and BS-2 collected during eleven days are shown in Fig. 9(a) and (b), respectively. As can be seen, there is a notable difference in the behavior of the BS clock offset between the two base stations. Whilst the difference between the maximum and minimum carrier phase measurement on BS-1 is 31.22 m as shown in Fig. 9(a), this difference is larger than 23 km on BS-2 as shown in Fig. 9(b).

2) Oscillator Frequency Jumps: To understand the behavior of the BS clock offset in more detail, the carrier phase measurements and drifts during selected intervals of 5000 s on BS-1 and BS-2 are shown in Fig. 10(a) and (b), respectively. The carrier phase drift is estimated by performing a linear regression of the carrier phase measurements over a 5 s sliding window and taking the slope of the regression. Fig. 10(a) and (b) show that the clock offset of both stations is driven by regular oscillator frequency jumps, which are sudden changes in the oscillator frequency. For

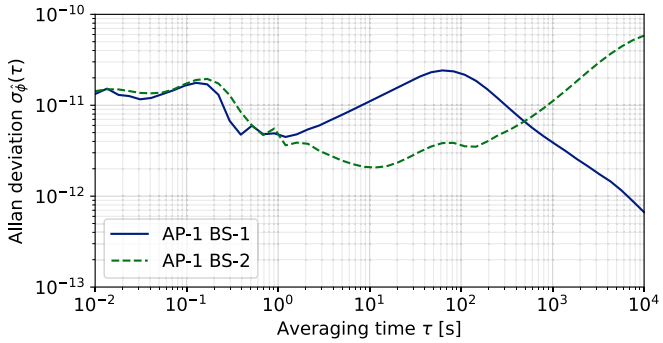

Fig. 11. Overlapping Allan deviation of BS-1 and BS-2 clocks computed using carrier phase measurements on AP-1.

example, as shown in Fig. 10(a), the first oscillator frequency jump that appears after epoch 226000 s causes a sudden change of the carrier phase drift from $\approx 0\,\mathrm{ms}^{-1}$ to almost $-0.3\,\mathrm{ms}^{-1}$ on BS-1. This results in the BS clock offset of almost -20 m before the oscillator frequency jumps again. As such, the oscillator frequency jumps are identified as the main contributor to the BS clock offset, making it of particular relevance for positioning as the resulting drifts of the code phase and carrier phase may introduce undesirable position errors if they are left uncorrected.

The exact mechanism causing the oscillator frequency jumps shown in Fig. 10 is not known. However, since the jumps occur at regular intervals, they could be caused by a periodic clock steering mechanism keeping the BS clocks synchronized to the primary clock reference to meet the 3GPP requirements. The jumps are more frequent on BS-1 than on BS-2, occurring roughly every minute on BS-1. The jumps in the carrier phase drift are also more severe and bounded on BS-1, whilst being more gradual and unbounded on BS-2. Small ripples of the carrier phase drift appear in Fig. 10(b) for BS-2, likely caused by small variations in the station clocks. According to [22], [23], the maximum carrier frequency error of a wide band BS shall be within ± 50 ppb over a period of 1 ms, corresponding to the worst drift of around $\pm 15\,\mathrm{ms}^{-1}$, or ± 1.5 cm over 1 ms. Both base stations remain within this requirement during the monitored period.

3) Frequency Stability: The frequency stability of the two monitored stations is analyzed and compared using the overlapping Allan deviation. Thanks to the use of a highly stable Rubidium reference clock in the monitoring setup, the Allan deviation from Section II-E can be computed for each station using the respective carrier phase measurements on AP-1. Low Allan deviation indicates a clock with good stability over the given averaging time. Fig. 11 shows that the clock stability is very similar on both stations for averaging times below ≈ 1 s. For averaging times between ≈ 1 s and ≈ 500 s, the clock stability of BS-1 is worse than that of BS-2. The clock stability of BS-1 becomes better than that of BS-2 for averaging times above ≈ 500 s. The differences in the clock stability between the stations coincide with the impact of the oscillator frequency jumps and could be a result of varying hardware or configuration.

4) Code-Carrier Coherence: The coherence of the BS clock offset between the code phase and carrier phase is analyzed by computing the CMC measure in (14). The CMC measures of BS-1 and BS-2 are shown in Fig. 12(a) and (b), respectively. For both stations, the CMC measure remains bounded and does not diverge, confirming that the BS clock offsets of the code phase and carrier phase are adjusted coherently and are thus impacted equally by the oscillator frequency jumps.

V. Impact of Base Station Clock Offset on Positioning

The impact of the BS clock offset on positioning is studied in a simulated terrestrial scenario in which the user navigates primarily with GNSS and relies on cellular signals to coast during GNSS unavailability. To allow positioning during coasting, the knowledge of the location and clock offset of each BS is needed. The UE is assumed to know the locations of the stations perfectly as their deployments are static and seldom change. However, as was observed in Section IV-C, the BS clock offset can change often, requiring prediction when GNSS becomes unavailable. It is assumed that the UE can perfectly estimate the BS clock offset when GNSS is available.

A. Clock Prediction Model

Similarly to real-time non-differential methods in GNSS, the BS clock offset can be estimated and predicted using a clock prediction model [24]. A clock prediction model works in two steps that are shown in Fig. 13. First, the clock model parameters are built by fitting the clock offset of each BS over a fitting interval τ_f [s]. This step is done by the UE during GNSS availability either with a dedicated model or as a part of the navigation filter. Second, the UE predicts the BS clock offset by extrapolating the estimated model over a coasting interval τ_c [s]. The extrapolated values allow the UE to correct the cellular measurements and use them for positioning during coasting. The clock prediction model assumed in this study is a linear polynomial defined as

$$x(t) = a_0 + a_1 t\,[\mathrm{s}], \tag{18}$$

where a_0 and a_1 are the model parameters. Although more complex models could be envisioned, the linear polynomial model is considered suitable when the BS clock offset is driven by the oscillator frequency jumps.

B. Clock Prediction Model Errors

The performance of the clock prediction model is evaluated using a realistic BS clock offset represented by the carrier phase measurements of AP-1 BS-1 and AP-1 BS-2 from Section IV-C. The performance of the clock model is evaluated for fitting intervals $\tau_\mathrm{f} \in \{1, 5, 10\}$ s and coasting intervals $\tau_\mathrm{c} \in \{1, 2, 5, 10, 20, 50, 100\}$ s. To evaluate the model over the full data set, the fitting and coasting intervals are sliding forwards every 0.5 s in each measurement set. Fitting and prediction are conducted and evaluated for each slide. The maximum clock prediction model errors for the evaluated fitting and coasting intervals are summarized in Table IV. Absolute values of the

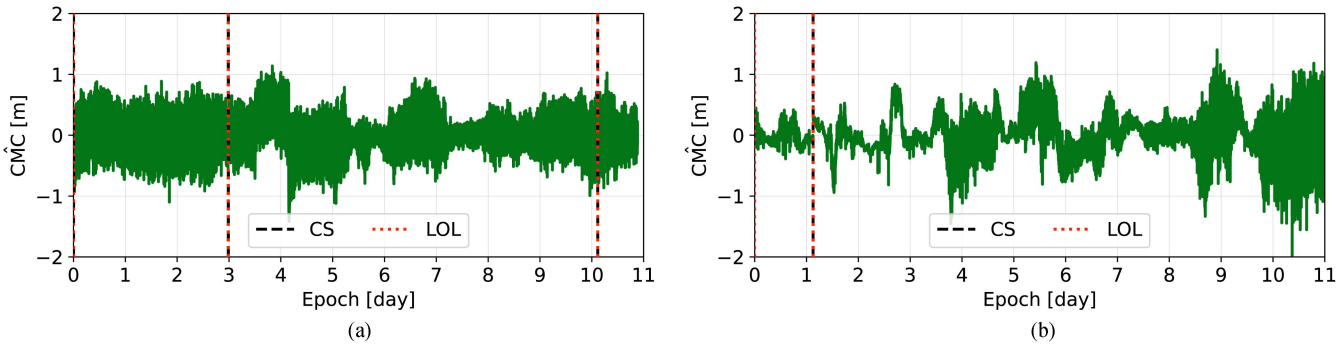

Fig. 12. Code-minus-carrier (CMC) measures on AP-1 BS-1 (a) and AP-1 BS-2 (b). The CMC measure is computed by subtracting the mean CMC value within a measurement set containing no cycle slip (CS) or loss of the signal lock (LOL) between consecutive epochs. The CMC measures are bounded and do not diverge, confirming that both monitored stations adjust the code phase and carrier phase coherently.

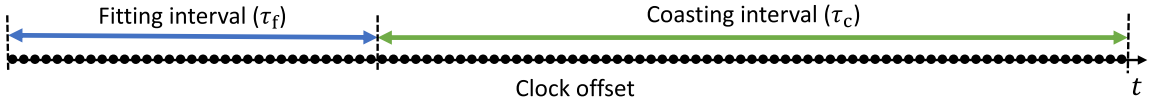

Fig. 13. Visualization of the operation of a clock prediction model. The fitting interval determines the BS clock offset series used by the UE to build the model during GNSS availability. When GNSS becomes unavailable, the UE predicts the BS clock offset by extrapolating the model over the coasting interval.

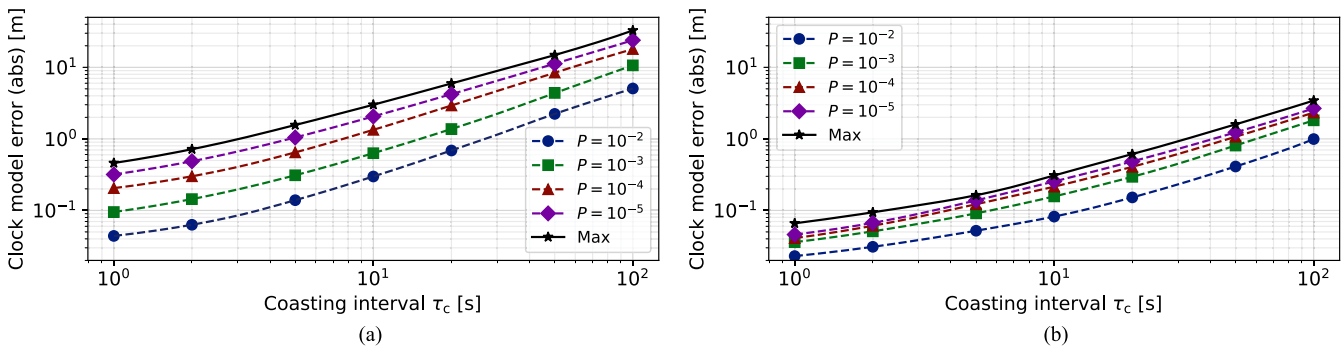

Fig. 14. Absolute values of the clock prediction model errors evaluated under various error probabilities on AP-1 BS-1 (a) and AP-1 BS-2 (b). The fitting interval is equal to $\tau_f = 5$ s.

TABLE IV
MAXIMUM ERRORS $\epsilon^{(\mathrm{MAX})}$ OF THE CLOCK PREDICTION MODEL EVALUATED WITH MEASUREMENTS FROM TWO BASE STATIONS (BS) FOR VARIOUS FITTING INTERVALS τ_f AND COASTING INTERVALS τ_c

BS	τ_f [s]	$\epsilon^{(\max)}$ [m]		
		$\tau_c = 1$ s	$\tau_c = 10$ s	$\tau_c = 100$ s
1	1	0.32	2.92	32.77
	5	0.46	3.00	32.77
	10	0.67	3.11	32.90
2	1	0.07	0.52	5.40
	5	0.07	0.31	3.43
	10	0.08	0.31	3.16

clock prediction model errors evaluated under various error probabilities are shown in Fig. 14(a) and (b) for BS-1 and BS-2, respectively.

Table IV shows that, for a given coasting interval, the model errors on BS-1 increase as the fitting interval increases. An opposite trend is observed on BS-2, as increasing the fitting interval reduces the errors for a given coasting interval. These results show that the optimal fitting interval of the clock prediction model is specific for a given BS. From the three evaluated fitting intervals, the BS clock offset of BS-1 and BS-2 can be best fitted with $\tau_f = 1$ s and $\tau_f = 10$ s, respectively. Table IV and Fig. 14 show that longer coasting intervals result in larger errors for both stations. This is in line with the expectation as a short coasting interval prevents the accumulation of errors caused by the oscillator frequency jumps. The residual clock prediction model errors are an order of magnitude larger on BS-1 than on BS-2 due to larger changes in the oscillator frequency on BS-1.

To understand the maximum duration for which the UE can rely on the clock prediction model not exceeding a certain error, the minimum and mean coasting intervals are evaluated for maximum model errors $\epsilon^{(\max)} \in \{0.1, 0.25, 0.5\}$ m, denoted respectively as E-10, E-25, and E-50. The results are summarized in Table V. As expected, a larger acceptable error allows for a longer coasting interval. The coasting intervals are shorter on BS-1 than on BS-2. On BS-1, the minimum observable coasting

TABLE V
MINIMUM $\tau_c^{(\mathrm{MIN})}$ AND MEAN $\tau_c^{(\mathrm{MEAN})}$ COASTING INTERVALS OF THE CLOCK PREDICTION MODEL EVALUATED WITH MEASUREMENTS FROM TWO BASE STATIONS (BS) FOR VARIOUS FITTING INTERVALS τ_f AND MAXIMUM CLOCK PREDICTION MODEL ERRORS (E-10, E-25, AND E-50)

BS	τ_f [s]	$\tau_c^{(\mathrm{min})}$ [s]			$\tau_c^{(\mathrm{mean})}$ [s]		
		E-10	E-25	E-50	E-10	E-25	E-50
1	1	0.2	1.2	1.7	52.9	90.5	112.3
	5	0.1	0.2	1.2	39.7	84.6	115.0
	10	0.1	0.1	0.2	21.1	56.6	97.7
2	1	2.5	7.6	17.0	48.0	117.4	243.5
	5	3.1	9.8	24.4	56.9	124.3	287.9
	10	2.6	11.2	21.4	56.4	118.1	279.7

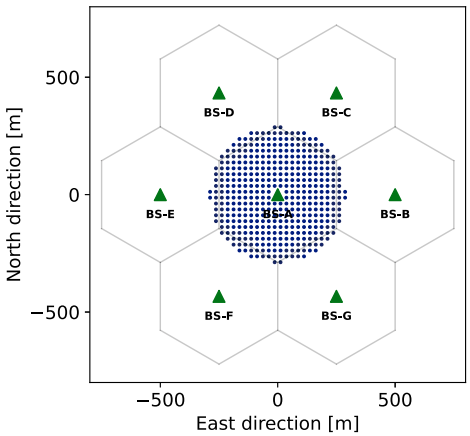

Fig. 15. Locations of seven base stations of a 5G NR terrestrial scenario used to evaluate the horizontal position error. The stations are deployed in a standard UMa hexagonal cellular layout with an inter-station distance of 500 m. Locations of the UEs are realized around BS-A located in the center with a minimum horizontal distance of 35 m and are shown as blue markers.

interval is limited by the evaluation step of 0.1 s as this duration is not always sufficient to bound the error. The probability of the clock prediction model having an error larger than $\epsilon^{(\max)} = 0.1$ m within 0.1 s is $P = 8.697 \times 10^{-2}$ and $P = 4.873 \times 10^{-1}$ for fitting intervals $\tau_f = 5$ s and $\tau_f = 10$ s, respectively. The probability of the clock prediction model having an error larger than $\epsilon^{(\max)} = 0.25$ m within 0.1 s is $P = 1.237 \times 10^{-1}$ for the fitting interval $\tau_f = 10$ s.

C. Simulation Methodology

To study the impact of the BS clock offset on positioning, the horizontal position error (HPE) is evaluated with a Monte Carlo simulation in a 5G NR terrestrial scenario with the urban macro (UMa) cellular deployment [1]. The scenario includes seven base stations deployed in a standard hexagonal layout shown in Fig. 15. The locations are expressed in local east, north, and up (ENU) coordinates. The inter-station distance (ISD) of the UMa deployment is 500 m. The height of the antenna phase center of each BS is set to $h_{\mathrm{BS}} = 25$ m. A static UE is placed in various places in the coverage of BS-A with a minimum horizontal distance to the BS-A equal to 35 m. The height of the UE antenna phase center is set to $h_{\mathrm{UE}} = 1.5$ m. The simulation was implemented in a custom Python 3 script using the NumPy

TABLE VI
PARAMETERS OF THE MONTE CARLO SIMULATION

Parameter	Value
Deployment geometry	
Inter-site distance (ISD) [m]	500
BS antenna phase center heigh h_{BS} [m]	25
UE antenna phase center heigh h_{UE} [m]	1.5
Link budget	
BS transmit power P_{T} [dBm]	49
BS antenna gain G_{T} [dBi]	8
UE antenna gain G_{R} [dBi]	0
UE noise floor NF [dB]	9
Thermal noise N_0 [dBm·Hz^{-1}]	-173.9
5G NR waveform	
Carrier frequency f_c [GHz]	5
Frequency range	FR1
Bandwidth B [MHz]	100
Numerology μ	1
Subcarrier spacing f_{sc} [kHZ]	30
Number of resource blocks $N_{\mathrm{sc}}^{\mathrm{RB}}$	273
Pilot subcarrier spacing ΔP	2
Number of pilots per bandwidth P	1638

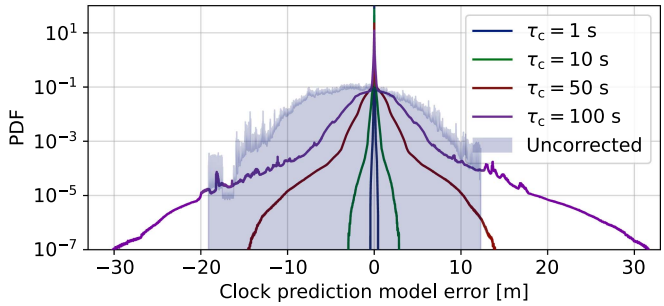

Fig. 16. Probability density functions (PDFs) of the residual clock prediction model errors on BS-1 for the fitting interval $\rho_f = 5$ s and various coasting intervals τ_c. The PDF of the uncorrected BS clock offset is also shown.

library. The script was configured with parameters for geometry, link budget, and 5G NR waveform that are summarized in Table VI. The details of the parameters and specific computations are provided in the next sections.

1) Modeling of Range Measurements: The range measurement R_m from the m-th BS is modeled as

$$R_m = \rho_m + \epsilon_{\mathrm{MRN}}(\rho_m) + \epsilon_{\mathrm{CB}}\ [\mathrm{m}], \tag{19}$$

where ρ_m is the geometric range between the antenna phase centers of the UE and the m-th BS, $\epsilon_{\mathrm{MRN}}(\rho_m)$ is the multipath and receiver noise error following a zero-mean Gaussian distribution with the variance $\sigma^2_{\mathrm{MRN}}(\rho_m)$, and ϵ_{CB} is the residual BS clock offset error following one of the probability density functions (PDFs) of the uncorrected or corrected BS clock offset. The PDFs were built using the results of AP-1 BS-1 for $\rho_f = 5$ s from Section V-B and are shown in Fig. 16. Only BS-1 is considered as its residual clock prediction model errors are an order of magnitude larger than those of BS-2. The residual BS clock offset error is assumed to be uncorrelated between the seven BS. The values of $\sigma^2_{\mathrm{MRN}}(\rho_m)$ are obtained as realizations of a log-normal distribution with the variance σ^2_{d} and mean μ_{d} equal

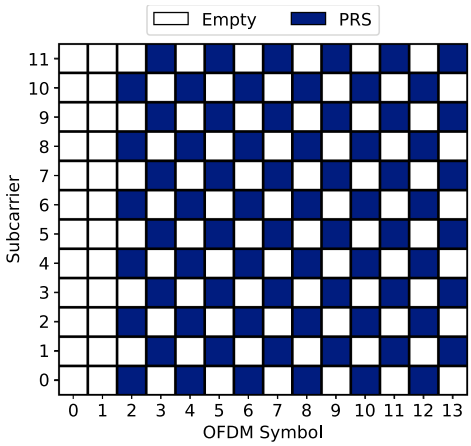

Fig. 17. Allocation of PRS pilots with the comb pattern 2/12 in a single resource block assumed in the simulation.

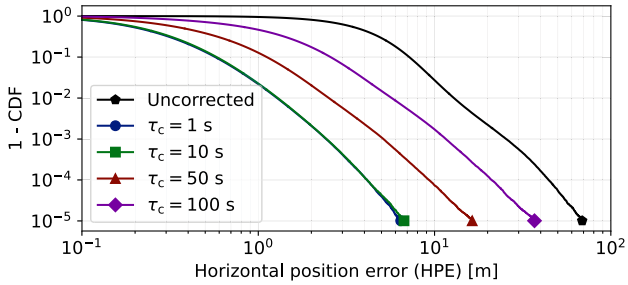

Fig. 18. Complementary cumulative density functions (1 - CDF) of the horizontal position error (HPE) evaluated in the UMa cellular deployment when the range measurements are either uncorrected or they are corrected with a clock prediction model for various coasting intervals τ_c.

to [42]

$$\mu_d(\rho_m) = \frac{c^2 n_0}{\mathrm{SNR}^{n_1}(\rho_m)\left(\sum_{p=0}^{P-1} f_{sc}^2 n_p^2\right)^{n_2}} \,[\mathrm{m}^2], \tag{20}$$

where n_0, n_1, and n_2 are the model parameters, $\mathrm{SNR}(\rho_m)$ is the signal-to-noise ratio, and f_{sc} is the subcarrier spacing. The model parameters are for the simulated UMa environment set to $n_0 = 10^{15.056}$, $n_1 = 0.37$, $n_2 = 0.65$, and $\sigma_d^2 = 2.18$ [42].

2) Link Budget: The SNR in (20) is modeled as

$$\begin{aligned}\mathrm{SNR}_{[\mathrm{dB}]}(\rho_m) &= P_T + G_T + G_R - L(\rho_m) - \mathrm{NF} \\ &\quad - N_0 - \log_{10}(B)\ [\mathrm{dB}],\end{aligned} \tag{21}$$

where P_T is the BS transmit power equal to 49 dBm, G_T is the BS antenna gain equal to 8 dBi, G_R is the UE antenna gain equal to 0 dBi, $L(\rho_m)$ is the distance-dependent path loss from [43], NF is the noise figure of the receiver equal to 9 dB, and N_0 is the thermal noise equal to -173.9 dBm $\cdot$ Hz^{-1}. Slow fading and inter-station interference effects are not modeled.

3) Positioning Reference Signal: The simulation assumes that each BS transmits a 5G NR waveform with the bandwidth of B $= 100$ MHz modulated on a carrier frequency $f_c = 5$ GHz. The numerology is $\mu = 1$, resulting in the subcarrier spacing of $f_{sc} = 30$ kHz and $N_{sc}^{RB} = 273$ available resource blocks [33]. The PRS is allocated in the comb pattern 2/12 with the pilot spacing $\Delta P = 2$ as shown in Fig. 17, resulting in $P = 1638$ available pilots over the full signal bandwidth. The OFDM subcarrier index of the p-th PRS pilot in (20) is computed as $n_p = p\,\Delta P - 6\,N_{sc}^{RB}$.

4) Positioning Algorithm: The UE is assumed to use range measurements from all seven BS for positioning. The positioning algorithm is based on the weighted least squares method where the displacement of the UE position from the linearization point $\Delta\hat{\mathbf{x}}$ is estimated as

$$\Delta\hat{\mathbf{x}} = (\mathbf{G}^T\mathbf{W}\mathbf{G})^{-1}\mathbf{G}^T\mathbf{W}\Delta\boldsymbol{\rho} \in \mathbb{C}^{n\times 1}, \tag{22}$$

where $\Delta\boldsymbol{\rho} = [\Delta\rho_0\,\Delta\rho_1 \ldots \Delta\rho_{M-1}]^T \in \mathbb{C}^{M\times 1}$ is a vector consisting of range measurements from M base stations minus the expected range values based on the location of the stations and the estimated location and receiver clock offset, $\Delta\hat{\mathbf{x}} = [\Delta x\,\Delta y\,\Delta z\,c\delta t]^T \in \mathbb{C}^{4\times 1}$ is the position and clock offset relative to the estimated location and clock offset of the UE expressed in local ENU coordinates, $\mathbf{G} = [\mathbf{g}_0\,\mathbf{g}_1 \ldots \mathbf{g}_{M-1}]^T \in \mathbb{C}^{M\times 4}$ is the Jacobian geometry matrix with $\mathbf{g}_m = [\frac{x_{UE}-x_{BS}}{\rho_m}\ \frac{y_{UE}-y_{BS}}{\rho_m}\ \frac{z_{UE}-z_{BS}}{\rho_m}\ 1]^T$, and $\mathbf{W} = \mathrm{diag}([w_0\,w_1 \ldots w_M]^T) \in \mathbb{C}^{M\times M}$ is the weighting matrix whose values on the diagonal are equal to the inverse of the error variance of a given BS from (19) as $w_m = \frac{1}{\sigma^2_{MRN}(\rho_m)}$, where it is assumed that the UE can estimate this variance perfectly. Although this assumption is optimistic, it serves to demonstrate the impact of the BS clock offset on the position error. The initial UE location is set to the real UE location and then iteratively updated using (22). At every iteration, any measurement with SNR < 10 dB is not considered in the positioning algorithm. If less than four measurements are available, the iteration is skipped.

D. Simulation Results and Discussion

The horizontal position error (HPE) is evaluated in 10^6 realizations of the simulation. Complementary cumulative density functions of HPE for various coasting times are shown in Fig. 18. As can be seen, large HPEs are observed when the clock is left uncorrected during coasting. HPE can be as large as 7.2 m and 68.8 m at $P = 10^{-1}$ and $P = 10^{-5}$, respectively. Depending on the coasting interval, the introduction of the clock prediction model can significantly reduce HPE when compared to the uncorrected clock offset. HPE for the coasting time of $\tau_c = 50$ s is reduced to 1.2 m and 16.4 m at $P = 10^{-1}$ and $P = 10^{-5}$, respectively. There is almost no difference in HPE between coasting intervals $\tau_c = 10$ s and $\tau_c = 1$ s, achieving HPE of ≈ 0.6 m and ≈ 6.5 m at $P = 10^{-1}$ and $P = 10^{-5}$, respectively. Since HPE depends on the number of stations and their geometry, the presented simulation is not representative of all possible deployments and serves mainly to demonstrate the relevance of the BS clock offset for positioning.

VI. Conclusion

The clock offset of two commercially operated LTE BS was studied using code phase and carrier phase measurements collected by a software receiver configured to track downlink cellular signals impacted by high clock dynamics. The carrier phase measurements were analyzed in terms of drifts and Allan deviation. The analysis revealed that the main contributor to the BS clock offset is the occurrence of regular oscillator frequency jumps. To mitigate the impact of the jumps on a user relying on cellular measurements to coast during GNSS unavailability, a clock prediction model was proposed and evaluated. It was shown that the model significantly reduces the HPE, especially for shorter coasting intervals. The CMC analysis showed that the monitored stations adjust the code phase and carrier phase coherently. The reported behavior of the station clocks highlights the importance of the BS clock offset for positioning and contributes to the characterization of cellular signals, which is needed to build the error models for integrity monitoring concepts in autonomous vehicle navigation. Although relevant observations of the BS clock behavior are made in this work, two stations and eleven days of monitoring are not generally representative of the diverse equipment and configuration of cellular network deployments.

Software and Data Availability

The source code of STARE is available from the European Space Software Repository (ESSR) under the terms of European Space Agency Software Community License Permissive (Type 3) - v2.4 at https://essr.esa.int/project/stare. The data used in this work belong to the European Space Agency and can be requested by contacting the corresponding author.

Acknowledgment

The authors would like to thank the Navigation Laboratory (NavLab) of the Directorate of Technology, Engineering, and Quality (TEC) at the European Space Agency for providing the premises and equipment for the monitoring setup.

References

[1] 3rd Generation Partnership Project, "Study on NR positioning support," Tech. Rep. 3GPP TR 38.855, V16.0.0, 3rd Generation Partnership Project, Sophia Antipolis, France, Mar. 2019.

[2] M. Driusso, C. Marshall, M. Sabathy, F. Knutti, H. Mathis, and F. Babich, "Vehicular position tracking using LTE signals," *IEEE Trans. Veh. Technol.*, vol. 66, no. 4, pp. 3376–3391, Apr. 2017.

[3] S. Kuutti, S. Fallah, K. Katsaros, M. Dianati, F. Mccullough, and A. Mouzakitis, "A survey of the state-of-the-art localization techniques and their potentials for autonomous vehicle applications," *IEEE Internet Things J.*, vol. 5, no. 2, pp. 829–846, Apr. 2018.

[4] C. Mensing, S. Sand, and A. Dammann, "Hybrid data fusion and tracking for positioning with GNSS and 3GPP-LTE," *Int. J. Navigation Observ.*, vol. 2010, pp. 1–12, 2010.

[5] G. De Angelis, G. Baruffa, and S. Cacopardi, "GNSS/cellular hybrid positioning system for mobile users in urban scenarios," *IEEE Trans. Intell. Transp. Syst.*, vol. 14, no. 1, pp. 313–321, Mar. 2013.

[6] J. A. Del Peral-Rosado et al., "Evaluation of hybrid positioning scenarios for autonomous vehicle applications," in *Proc. 30th Int. Tech. Meeting Satell. Division Inst. Navigation*, 2017, pp. 2541–2553.

[7] N. Zhu, J. Marais, D. Bétaille, and M. Berbineau, "GNSS position integrity in urban environments: A review of literature," *IEEE Trans. Intell. Transp. Syst.*, vol. 19, no. 9, pp. 2762–2778, Sep. 2018.

[8] M. Jia, J. Khalife, and Z. M. Kassas, "Evaluation of ground vehicle protection level reduction due to fusing GPS with faulty terrestrial signals of opportunity," in *Proc. Int. Tech. Meeting Inst. Navigation ITM*, 2021, pp. 354–365.

[9] M. Maaref and Z. M. Kassas, "Autonomous integrity monitoring for vehicular navigation with cellular signals of opportunity and an IMU," *IEEE Trans. Intell. Transp. Syst.*, vol. 23, no. 6, pp. 5586–5601, Jun. 2022.

[10] F. Rothmaier and J. A. Del Peral Rosado, "A parametric study on autonomous integrity monitoring using non-GNSS signals," in *Proc. IEEE/ION Position, Location Navigation Symp.*, 2023, pp. 1154–1161.

[11] Y. Sun, L. Cao, S. Li, and Z. Deng, "G5GIM: Integrity monitoring for GNSS/5G integrated navigation of urban vehicles," *IEEE Trans. Instrum. Meas.*, vol. 72, 2023, Art. no. 3524513.

[12] "GNSS European (GALILEO) open service - service definition document," European Union Standard, Rev. 1.1, May 2019.

[13] "Global positioning system - standard positioning service (SPS) - performance standard," U.S. Department of Defense, VA, USA, Tech. Rep. Apr. 2020. [Online]. Available: https://www.gps.gov/technical/ps/2020-SPS-performance-standard.pdf

[14] A.-E. William J. Hughes Technical Center, Satellite Navigation Branch, "Advanced receiver autonomous integrity monitoring performance analysis report," United States (U.S.) Federal Aviation Administration (FAA), Washington, DC, USA, Tech. Rep., Jul. 2022. [Online]. Available: https://www.nstb.tc.faa.gov/reports/2021_Q2_araim_report_v1.0.pdf

[15] M. T. Alonso, J. Sanz, J. M. Juan, A. Rovira García, and G. G. Casado, "Galileo broadcast ephemeris and clock errors analysis: 1 Jan. 2017 to 31 Jul. 2020," *Sensors*, vol. 20, no. 23, 2020, Art. no. 6832.

[16] K. Gunning, T. Walter, and P. Enge, "Characterization of GLONASS broadcast clock and ephemeris: Nominal performance and fault trends for ARAIM," in *Proc. Int. Tech. Meeting Inst. Navigation*, Monterey, 2017, pp. 170–183.

[17] L. Heng, G. X. Gao, T. Walter, and P. Enge, "GPS signal-in-space integrity performance evolution in the last decade," *IEEE Trans. Aerosp. Electron. Syst.*, vol. 48, no. 4, pp. 2932–2946, Oct. 2012.

[18] Working Group C. - ARAIM Technical Subgroup, "EU-U. S. cooperation on satellite navigation, milestone 3 report," Tech. Rep. Final Version, Feb. 2016. [Online]. Available: https://www.gps.gov/policy/cooperation/europe/2016/working-group-c/ARAIM-milestone-3-report.pdf

[19] P. Brieden et al., "Galileo characterization as input to H-ARAIM and SBAS DFMC," in *Proc. 32nd Int. Tech. Meeting Satell. Division Inst. Navigation*, 2019, pp. 2819–2841.

[20] International Civil Aviation Organization (ICAO), Standards And Recommended Practices (SARPs), Annex 10 - Aeronautical Telecommunications - Volume I - Radio Navigational Aids, Eight Edition, Jul. 2023. [Online]. Available: https://store.icao.int/en/annex-10-aeronautical-telecommunications-volume-i-radio-navigational-aids

[21] E. Kaplan and C. Hegarty, *Understanding GPS/GNSS: Principles and Applications.*, 3rd ed., Norwood, MA, USA: Artech House, 2017.

[22] 3rd Generation Partnership Project, "NR; Base Station (BS) radio transmission and reception," 3rd Generation Partnership Project, Sophia Antipolis, France, Tech. Specification, 3GPP TS 38.104, V18.4.0, Dec. 2023.

[23] 3rd Generation Partnership Project, "Evolved universal terrestrial radio access (E-UTRA); base station (BS) radio transmission and reception," 3rd Generation Partnership Project, Sophia Antipolis, France, Tech. Specification, 3GPP TS 36.104, V18.4.0, Dec. 2023.

[24] H. Ge, B. Li, T. Wu, and S. Jiang, "Prediction models of GNSS satellite clock errors: Evaluation and application in PPP," *Adv. Space Res.*, vol. 68, no. 6, pp. 2470–2487, 2021.

[25] A. Winter, A. Morrison, and N. Sokolova, "Analysis of 5G and LTE signals for opportunistic navigation and time holdover," *Sensors*, vol. 24, no. 1, 2024, Art. no. 213.

[26] B. Camajori Tedeschini et al., "A feasibility study of 5G positioning with current cellular network deployment," *Sci. Rep.*, vol. 13, no. 1, 2023, Art. no. 15281.

[27] J. A. Del Peral-Rosado et al., "Software-defined radio LTE positioning receiver towards future hybrid localization systems," in *Proc. 31st AIAA Int. Commun. Satell. Syst. Conf.*, 2013, pp. 1–11.

[28] J. A. D. Peral-Rosado et al., "Comparative results analysis on positioning with real LTE signals and low-cost hardware platforms," in *Proc. IEEE 7th ESA Workshop Satell. Navigation Technol. Eur. Workshop GNSS Signals Signal Process.*, 2014, pp. 1–8.

[29] K. Shamaei, J. Khalife, and Z. M. Kassas, "Performance characterization of positioning in LTE system," in *Proc. 29th Int. Tech. Meeting Satell. Division Inst. Navigation*, 2016, pp. 2262–2270.

[30] K. Shamaei and Z. M. Kassas, "LTE receiver design and multipath analysis for navigation in urban environments," *Navigation*, vol. 65, no. 4, pp. 655–675, 2018.
[31] K. Shamaei and Z. M. Kassas, "Receiver design and time of arrival estimation for opportunistic localization with 5G signals," *IEEE Trans. Wireless Commun.*, vol. 20, no. 7, pp. 4716–4731, Jul. 2021.
[32] I. Lapin, G. S. Granados, J. Samson, O. Renaudin, F. Zanier, and L. Ries, "STARE: Real-time software receiver for LTE and 5G NR positioning and signal monitoring," in *Proc. IEEE 10th Workshop Satell. Navigation Technol.*, 2022, pp. 1–11.
[33] 3rd Generation Partnership Project, "NR; physical channels and modulation," Tech. Specification 3rd Generation Partnership Project, Sophia Antipolis, France, Technical Specification TS 38.211, V18.1.0, Dec. 2023.
[34] 3rd Generation Partnership Project, "Evolved universal terrestrial radio access (E-UTRA); physical channels and modulation," 3rd Generation Partnership Project, Sophia Antipolis, France, Tech. Specification, 3GPP TS 36.211, V17.4.0, Sep. 2023.
[35] W. Xu, M. Huang, C. Zhu, and A. Dammann, "Maximum likelihood TOA and OTDOA estimation with first arriving path detection for 3GPP LTE system," *Trans. Emerg. Telecommun. Technol.*, vol. 27, no. 3, pp. 339–356, 2014.
[36] K. Shamaei, J. Khalife, and Z. M. Kassas, "Comparative results for positioning with secondary synchronization signal versus cell specific reference signal in LTE systems," in *Proc. Int. Tech. Meeting Inst. Navigation*, 2017, pp. 1256–1268.
[37] L. Chen, P. Thevenon, G. Seco-Granados, O. Julien, and H. Kuusniemi, "Analysis on the TOA tracking with DVB-T signals for positioning," *IEEE Trans. Broadcast.*, vol. 62, no. 4, pp. 957–961, Dec. 2016.
[38] B. Yang, K. B. Letaief, R. S. Cheng, and Z. Cao, "Timing recovery for OFDM transmission," *IEEE J. Sel. Areas Commun.*, vol. 18, no. 11, pp. 2278–2291, Nov. 2000.
[39] K. Shamaei and Z. M. Kassas, "Sub-meter accurate UAV navigation and cycle slip detection with LTE carrier phase measurements," in *Proc. 32nd Int. Tech. Meeting Satell. Division Inst. Navigation*, 2019, pp. 2469–2479.
[40] W. J. Riley, "Handbook of frequency stability analysis," National Institute of Standards and Technology, U.S. Department of Commerce, 2008. [Online]. Available: https://www.nist.gov/publications/handbook-frequency-stability-analysis
[41] Antennebureau, "Dutch antenna register (Antenneregister)," Accessed: Aug. 2021. [Online]. Available: https://antenneregister.nl
[42] O. Renaudin, J. A. López-Salcedo, G. Seco-Granados, I. Lapin, F. Zanier, and L. Ries, "TOA error bounds for positioning in 5G new radio networks," in *Proc. 34th Int. Techn. Meeting Satell. Division Inst. Navigation*, 2021, pp. 2940–2956.
[43] 3rd Generation Partnership Project, "Study on channel model for frequencies from 0.5 to 100 GHz," 3rd Generation Partnership Project, Sophia Antipolis, France, Tech. Report, 3GPP TR 38.901, V17.0.0, Mar. 2022.

Ivan Lapin received the M.Sc. and Ph.D. degrees in telecommunications from the Slovak University of Technology, Bratislava, Slovakia. In 2016, he joined the European Space Agency (ESA), Noordwijk, The Netherlands, as an EGNOS System Performance Engineer. He is currently a Radio Navigation System Engineer with the Radio Navigation Systems and Techniques Section with ESA, where he is involved in the topics of LEO-PNT, 5G/6G PNT, multi-layer PNT, radio navigation space receivers, and SBAS data authentication. His research interests include positioning with 5G/6G terrestrial and non-terrestrial networks, multi-layer PNT, signal processing, radio navigation space receivers, and integrity monitoring.

Gonzalo Seco-Granados (Fellow, IEEE) received the M.B.A. degree from the IESE Business School, Barcelona, Spain, in 2002, and the Ph.D. degree in telecommunications engineering from the Universitat Politecnica de Catalunya, Barcelona, in 2000. From 2002 to 2005, he was a member of the European Space Agency, Noordwijk, The Netherlands, where he was involved in the design of the Galileo system and receivers. In 2015, 2019, and 2022, he was a Fulbright Visiting Scholar with the University of California, Irvine, CA, USA. He is currently a Professor with the Department of Telecommunication, Universitat Autonoma de Barcelona, Bellaterra, Spain, where he was the Vice Dean of the Engineering School during 2011–2019. His research interests include localization based on GNSS and 5G systems. Since 2018, he has been a member of the Sensor Array and Multichannel Technical Committee for the IEEE Signal Processing Society. Since 2019, he has been the President of the Spanish Chapter of the IEEE Aerospace and Electronic Systems Society.

Jaron Samson received the M.Sc. degree in physical and mathematical geodesy from the Delft University of Technology, Delft, The Netherlands. In 2003, he joined the European Space Agency (ESA), Noordwijk, The Netherlands. From 2012 to 2020, he was an EGNOS System Engineer with ESA's EGNOS Project Office, Toulouse, France. He is currently a Radio Navigation System Engineer with ESA/ESTEC.

José Antonio Garcia-Molina received the M.Sc. and Ph.D. degrees in telecommunications engineering from the Universitat Politecnica de Catalunya, Barcelona, Spain. He is currently the Head with the Radio Navigation Systems and Techniques Section, European Space Agency (ESA), Noordwijk, The Netherlands, where he leads the team shaping the future of PNT systems, signals, receivers and techniques with ESA, contributing to the evolution of Galileo/G2G, LEO-PNT, Multi-layer PNT, Hybrid 5G/6G-GNSS, Moonlight, EGNOS, space receivers, and R&D programmes. In 2012, he joined ESA where he has led R&D activities on GNSS/Galileo receiver and signal processing techniques for ground and space applications, and is leading the Galileo 2nd Generation signal-in-space evolution. His research interests include signal processing and estimation theory, GNSS/Galileo system and signal design evolution, Multi-layer PNT and LEO-PNT, PNT in harsh propagation conditions, MIMO-GNSS signal processing, collaborative positioning, and meta-signal processing.